

Deep-learning-based separation of shallow and deep layer blood flow rates in diffuse correlation spectroscopy

MIKIE NAKABAYASHI,^{1,†} SIWEI LIU,^{1,†} NAWARA MAHMOOD BROTI,¹
MASASHI ICHINOSE,² AND YUMIE ONO^{3,*} 

¹Electrical Engineering Program, Graduate School of Science and Technology, Meiji University, 1-1-1 Higashi-Mita, Tama-ku, Kawasaki, Kanagawa, 2148571, Japan

²Human Integrative Physiology Laboratory, School of Business Administration, Meiji University, 1-1 Surugadai, Kanda, Chiyoda-ku, Tokyo, 1018301, Japan

³Department of Electronics and Bioinformatics, School of Science and Technology, Meiji University, 1-1-1 Higashi-Mita, Tama-ku, Kawasaki, Kanagawa, 2148571, Japan

[†]These authors contributed equally to this work.

*yumie@meiji.ac.jp

Abstract: Diffuse correlation spectroscopy faces challenges concerning the contamination of cutaneous and deep tissue blood flow. We propose a long short-term memory network to directly quantify the flow rates of shallow and deep-layer tissues. By exploiting the different contributions of shallow and deep-layer flow rates to auto-correlation functions, we accurately predict the shallow and deep-layer flow rates (RMSE = 0.047 and 0.034 ml/min/100 g of simulated tissue, $R^2 = 0.99$ and 0.99, respectively) in a two-layer flow phantom experiment. This approach is useful in evaluating the blood flow responses of active muscles, where both cutaneous and deep-muscle blood flow increase with exercise.

© 2023 Optica Publishing Group under the terms of the [Optica Open Access Publishing Agreement](#)

1. Introduction

Diffuse correlation spectroscopy (DCS) is an optical measurement technique used to quantify tissue blood flow, and it has shown great potential in both medical [1–5] and sports physiology [6–12] applications due to its non-invasive and cost-effective nature. The blood flow index (BFI) is used to estimate the tissue blood flow, a parameter representing the mean square displacement of red blood cells per second. Previous studies have demonstrated a strong correlation between BFI and the tissue blood flow rate as measured using perfusion magnetic resonance imaging [13] and bolus tracking methods [3,14].

Traditionally, DCS quantifies BFI values by fitting the photon-intensity autocorrelation function, which is observed at the target tissue surface, to theoretical model equations [15]. However, the commonly used model assumes the tissue to be a homogeneous, semi-infinite medium. While this model effectively provides reasonable information concerning tissue blood flow in practical DCS measurements, anatomical tissue structures and hemodynamic responses across different tissue layers may alter the measured morphology of autocorrelation functions and lead to the misinterpretation of the blood flow dynamics.

One potential example of a complex blood flow response caused by tissue heterogeneity is active muscle measurements. During exercise, blood flow to both active muscles and skin increases to meet the oxygen demand of active muscles and to dissipate the generated heat. As photons pass through both the shallow cutaneous and deep muscle layers before being captured by the detector optode, the detected light may reflect blood flow information from both tissue layers. Moreover, the BFI values obtained from the surface of an exercising limb have been reported to be significantly affected by the exercise-induced enhancement of cutaneous blood flow [11,12], which may prevent the accurate quantification of muscle blood flow. Although local

cooling or pharmacological blockades are promising methods for evaluating muscle blood flow while minimizing the effect of cutaneous blood flow on BFI values [10–12], these techniques may not be suitable for some patient/elderly populations and repetitive measurement settings. The complex contributions of different tissue layers may not be accurately captured by simple model equations that assume a homogeneous blood flow pattern. More advanced strategies are required to evaluate multi-layer blood flow [16–19].

Previous studies have shown the usefulness of deep learning frameworks in DCS research, such as denoising the autocorrelation function and directly calculating the BFI. Zhang et al. [20] proposed a deep learning recurrent neural network (RNN) regression model for denoising autocorrelation functions. Feng et al. [21] estimated relative cerebral blood flow using a combined convolutional neural network (CNN) and RNN model. Li et al. [22,23] proposed a deep neural network with a long short-term memory (LSTM) architecture for calculating blood flow and oxygen saturation from both phantom and *in vivo* models. Poon et al. [24] used MobileNetV2, a lightweight CNN architecture, to quantify blood-flow-related parameters and assess blood flow changes during an arm cuff ischemia in a human participant. However, none of these models have considered the anatomical composition of the target tissue, such as the cutaneous and muscle layers, which can have different hemodynamic responses due to microvascular density, temperature, and exercise conditions. Therefore, the current study aimed to investigate the potential of using deep-learning-based methods for distinguishing the blood flow rates of shallow and deep layers from autocorrelation functions obtained at the tissue surface.

The remainder of the paper is organized as follows. First, we describe our two-layer phantom flow model, which was used to collect DCS data under the independent control of flow rates in shallow and deep layers. Next, we detail the DCS instrumentation and experimental protocols used to collect the autocorrelation function from the flow phantom. We then provide a procedure for utilizing a deep neural network with LSTM that is employed to predict flow rates in both shallow and deep layers from the autocorrelation function. We present and discuss the results considering comparisons of the autocorrelation function with varied flow rates in the two layers, their correspondence to the BFI values, and the prediction accuracy of flow rates by the proposed LSTM network-based method. Finally, we conclude by summarizing the main contributions of this study and providing suggestions for future research.

2. Methods

2.1. Two-layer phantom flow model

We fabricated a flow phantom model (Fig. 1(ab)) that can independently modulate the flow rate of the two-layered compartments used in this experiment. The phantom was made of acrylic resin (AR-M2; Keyence) with dimensions of $100 \times 50 \times 50.5$ mm in length, width, and height, respectively, with the longest side serving as the flow direction. It was manufactured using a 3D printer and filled with glass beads (diameter: 2.5 to 3.5 mm; BZ-2, AXEL, Japan) without gaps. This flow model has been verified to approximate photon propagation *in vivo*, where photon scattering from moving scatterers has been observed to exhibit Brownian motion [25]. A Mylar sheet (thickness: 0.05 mm) separated the upper and lower layers, which had depths of 5.5 and 35 mm, respectively. The depth of the upper layer was determined according to the mean depth of the medial head of the gastrocnemius muscle in 25 young adults measured by an ultrasonic diagnostic imaging apparatus (MUS-P0301-L75, ITO Physiotherapy & Rehabilitation, Japan). The surface of the upper layer was also sealed with the same Mylar sheet to which we attached the DCS probes. Each phantom layer had an inlet connected to a programmable syringe pump (FP-2200, Melquest, Japan) and an outlet fixed to a plastic container above the mass meter. We used the mass meter to weigh the outgoing fluid every 30 s to measure the exact flow rates of the upper and lower layers. As the upper and lower layers simulate the shallow, cutaneous tissue and

the deep, muscle tissue layers of the living body, hereinafter we refer to them as the shallow and deep layers, respectively.

To simulate blood flow, we used a mixture of 20 μL of India ink (BD3-18; Kuretake, Japan) and 40 ml of a 20% intralipid solution (Otsuka Pharmaceutical, Japan), which was distilled in 1 L of tap water and used as the fluid in the phantom chamber. The absorption coefficient (μ_a) and reduced scattering coefficient (μ'_s) of the phantom filled with this fluid were measured using the time-resolved spectroscopy system (TRS-20; Hamamatsu Photonics, Japan) at wavelengths of 760 and 800 nm with a source-detector separation of 3 cm. The μ_a and μ'_s values at a wavelength of 785 nm were estimated as the average of the coefficients measured at the above wavelengths and were 0.56 and 4.81 cm^{-1} , respectively.

2.2. DCS instrumentation

We used a 785-nm, long-coherent continuous-wave laser (DL-785-100-S, CrystaLaser, NV, USA) and a four-channel single-photon counting module (SPCM-C, Excelitas, MA, USA) to construct our DCS system [6,10,26–28]. The near-infrared light emitted was transmitted through a multimode fiber (FT400EMT, Thorlabs Japan Inc. Japan) and directed towards the surface of the phantom. The diffused light was detected by a single-mode fiber (S630-HP, Thorlabs, Japan) positioned at distances of 1, 2, and 3 cm from the source fiber. The collected light intensity was measured using a 32-bit counter board (USB-6341, National instruments Co., Japan). The sampling rate of the photon intensity was 1 MHz when the flow rate of either layer was faster than 30 ml/min/100 g of tissue and 400 kHz otherwise. The 1 MHz sampling rate was used to capture the faster decay of the autocorrelation function and the 400 kHz sampling rate was used to improve the signal-to-noise ratio of the light intensity data. The autocorrelation function calculated from the light intensity data sampled at 400 kHz was up-sampled to 1 MHz for further analysis using the deep learning model.

2.3. Protocols and experiments

We conducted a phantom experiment where we collected 1340 autocorrelation functions $g_2(r, \tau)$ of the normalized light intensity (Eq. (1)) with varying combinations of flow rates for both shallow and deep layers. $g_2(r, \tau)$ was computed every second from the detected light intensity $I(r, t)$, where r, t, τ , and brackets $\langle \rangle$ represent the position, time, delay from t , and time-averages, respectively.

$$g_2(r, \tau) = \frac{\langle I(r, t) * I(r, t + \tau) \rangle}{\langle I(r, t) \rangle^2} \quad (1)$$

The 134 combinations of the shallow and deep layer flow rates were set across rates from 0 to 70 ml/min/100 g of simulated tissue (0, 1, 2, 3, 4, 5, 6, 7, 9, 10, 11, 13, 14, 15, 20, 25, 30, 35, 40, 45, 50, 55, 60, 65, and 70 ml/min/100 g of simulated tissue; Fig. 1(c)). These flow rates were chosen to simulate the physiological ranges of cutaneous and muscle blood flow during a resting state and exercise [29–36]. We maintained each combination of shallow- and deep-layer flow rates for 1 min and averaged the measurements taken during the 1-min-interval to determine the single trial $g_2(r, \tau)$ data. We then paired each data point with the measured flow rates of the shallow and deep layers by weighing the outlet liquid volumes. For each combination of shallow- and deep-layer flow rates, we measured the $g_2(r, \tau)$ data for 10 times.

We calculated the normalized electric field autocorrelation function $g_1(r, \tau)$ to the 10 ms delay time to clearly visualize the changes in their decay slopes, which are equivalent to the BFI (Eq. (2)). We derived $g_1(r, \tau)$ from $g_2(r, \tau)$ using the following Siegert relation normalized to the intensity of light [15]:

$$g_2(r, \tau) = 1 + \beta |g_1(r, \tau)|^2 \quad (2)$$

where β is derived from the analytical model fit (Eq. (3) in Section 2.4.1) of each observation.

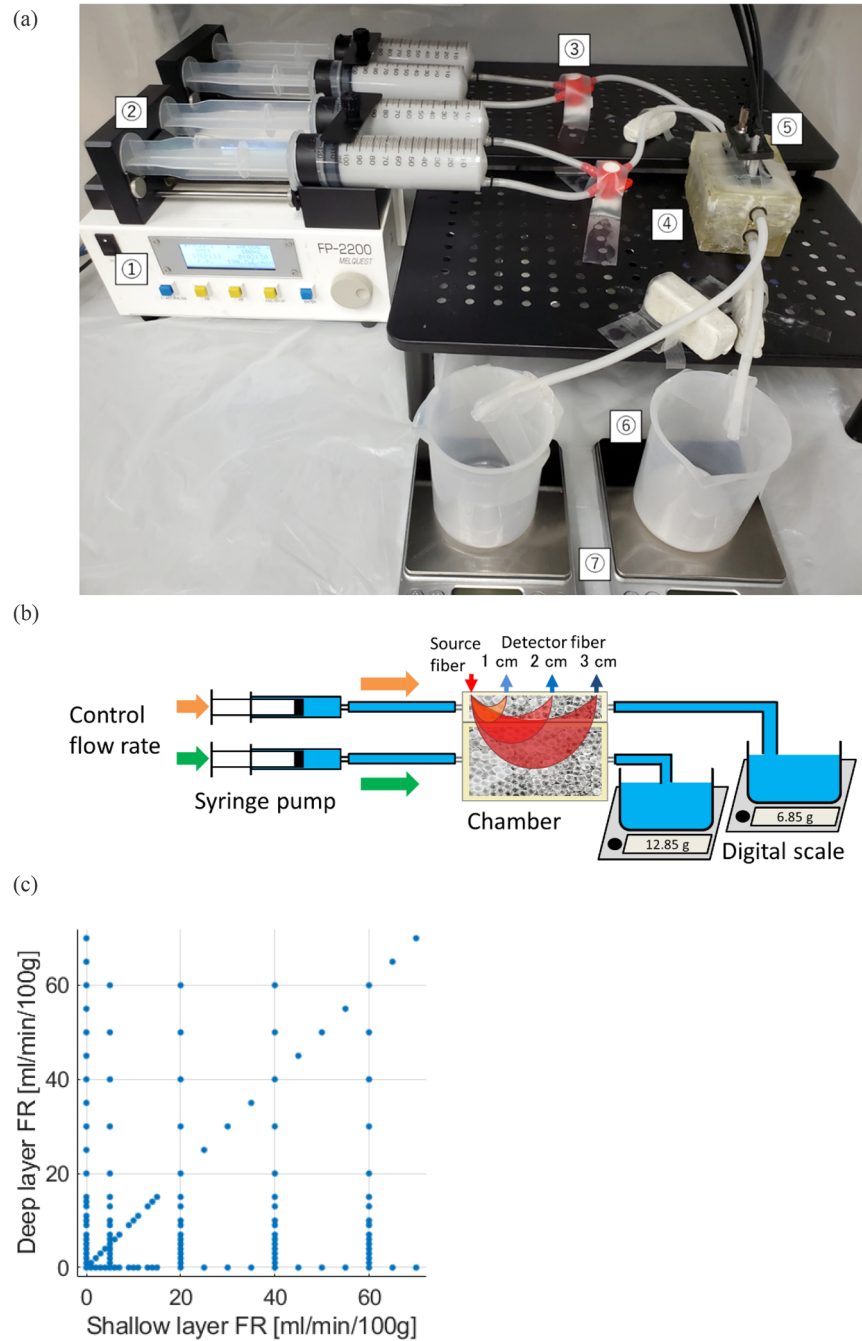


Fig. 1. (a) Overview, (b) schematic representation, and (c) tested flow rate combinations of the flow phantom system. (a) Two programmable syringe pumps (1) eject the intralipid solutions filled in the syringes (2). A three-way stopcock (3) is placed between the syringe and phantom (4) to prevent backflow. The DCS probes of source-detector separations of 1, 2, and 3 cm (5) were attached to the top of the phantom. The outflow was guided to the plastic containers (6) placed on the mass meter (7) to weigh the outlet liquid volume of each layer of the phantom. (b) The flow rates of two layers were independently controlled by two syringe pumps. (c) Scatter plot displaying the 134 combinations of shallow and deep layer flow rates (FR) set at the syringe pumps.

2.4. Data analysis

We used two different methods to analyze the obtained data: the conventional model-fit method (section 2.4.1) and the proposed deep-learning-based method (section 2.4.2). The delay of the autocorrelation functions was varied from 0 to 500 μs for the following analyses.

2.4.1. BFI estimation

The BFI is a relative measure of the average blood flow speed within a tissue volume that emitted light has traveled through. BFI values were obtained using a fast Fourier transform-based software autocorrelator from the time-based variation of the light intensity [15,25]. To determine the BFI, $g_2(r, \tau)$ was fitted to the theoretical autocorrelation function $G_2(r, \tau)$ derived from the Green's function solution of the diffusion correlation equation, in which case the model was considered as a point light source on the semi-infinite plate medium [15,25], as shown in Eq. (3):

$$G_2(r, \tau) = 1 + \beta \frac{\left| \frac{3\mu'_s}{4\pi} \left(\frac{e^{-k_D r_1}}{r_1} - \frac{e^{-k_D r_2}}{r_2} \right) \right|^2}{I(r, t)^2} \quad (3)$$

where $k_D = \sqrt{3\mu'_s\mu_a + 6\mu'_s{}^2 k_0^2 \alpha D_B \tau}$, $r_1 = \sqrt{\rho^2 + z_0^2}$, $r_2 = \sqrt{\rho^2 + (z_0 + 2z_b)^2}$, $z_0 = \mu'_s{}^{-1}$, and $z_b = 2(1 - R_{eff})/3\mu'_s(1 + R_{eff})$. Here, β is a constant, α is the fraction of photon scattering events of moving scatterers in the total amount of scatterers, k_0 is the wavenumber of the light in a medium, D_B is the effective diffusion coefficient of the scatterers, R_{eff} is the effective reflection coefficient, and ρ is the source-detector separation. We defined αD_B as the BFI according to the Brownian motion characteristics of the moving scatterers within the flow phantom using glass beads [25].

For each source-detector separation condition (1, 2, and 3 cm), we determined the BFI value from the $g_2(r, \tau)$ data measured under 1340 combinations of shallow and deep-layer flow rates. Because the flow rates of the shallow and deep layers have varying impacts on the calculated BFI values detected at different source-detector separation distances, we conducted a linear regression analysis to explore the relationship between the detected BFI value and the flow rates of the shallow and deep layers for each condition of source-detector separation. We determined the coefficients c_i ($i = 1, 2, 3$) of the following linear relationship between the BFI and the flow rates of the shallow ($FR_{shallow}$) and deep (FR_{deep}) layers using the least squares method:

$$BFI = c_1 \cdot FR_{shallow} + c_2 \cdot FR_{deep} + c_3 \quad (4)$$

We evaluated the coefficients of determination (R^2 values) as an index of the goodness of fit of the model.

2.4.2. Shallow and deep-layer flow rate estimation using an LSTM network

The $g_2(r, \tau)$ dataset consists of 1340 trials, each of which has 3×501 data points (3 source-detector separations \times 501 delay time points). Therefore, the total dataset size is 4020×501 . We employed a 90-10 split to partition the dataset, with randomly selected 90% of the data used for training and the remaining 10% used for testing. Since there were 10 observations each for 134 combinations of shallow and deep layer flow rates, we randomly selected nine of them for training and the remaining one for testing for each combination of flow rate settings. Therefore, the training data includes 1206 trials with a size of 3618×501 , while the test data includes 134 trials with a size of 402×501 .

LSTM is a type of RNN architecture designed to handle sequential data by capturing long-term dependencies. Unlike traditional RNNs, LSTM introduces a memory cell that can store information over extended periods. It can selectively remember or forget past information while

retaining information relevant to the current task. This selective memory mechanism makes LSTM well-suited for sequential data and has been shown to achieve state-of-the-art performance on a wide range of sequential data tasks, including the quantification of BFI from $g_2(r, \tau)$ [22].

The proposed LSTM architecture used in this study is illustrated in Fig. 2. The input to the model consists of the measured $g_2(r, \tau)$ data at three different source-detector separations, which are set as three 1×501 vectors for each trial. Before being included in the model, the $g_2(r, \tau)$ variables are normalized using z-scores. Each 1×501 segment is then divided into three sections that represent the prior, middle, and post periods of the autocorrelation function, resulting in three 1D signals of size 1×167 . These signals are fed sequentially to two LSTM hidden layers, each containing 512 LSTM units. Finally, a fully connected layer of size 1×2 uses the softmax classifier to generate the predicted flow rate values. The output of the model is a 1×2 vector that represents the predicted blood flow rates for the shallow and deep layers. To capture the detailed temporal features specific to the flow rates of shallow and deep layers, we made technical refinements to the method used in a previous study [22]. Specifically, we prolonged the length of the autocorrelation function and its segmentation, which are subjected to the LSTM layers. The single autocorrelation function is divided into three segments to utilize all the information of the autocorrelation function while reducing the computational complexity. Furthermore, we increased the number of LSTM units in each LSTM layer.

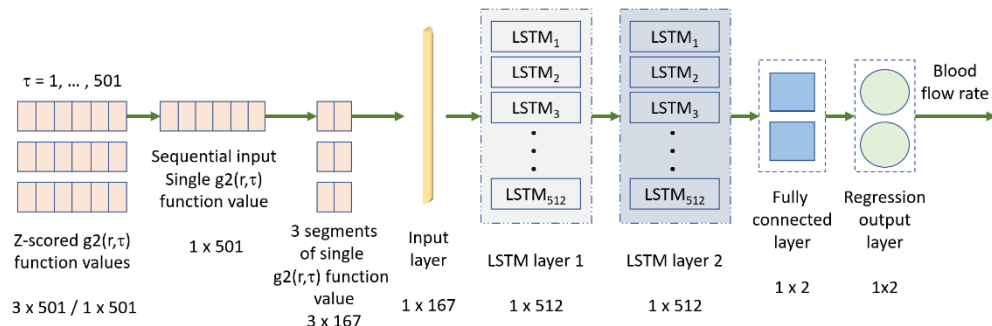


Fig. 2. Proposed LSTM model structure

We also examined the detection of flow rates for the shallow and deep layers with input data consisting of the measured $g_2(r, \tau)$ data from a single source-detector separation, as both the shallow and deep layers have different effects on the time-decay patterns of $g_2(r, \tau)$ even when the predicted BFI value is almost the same (see Section 3.2 for a detailed description). In this scenario, each trial is represented by a single 1×501 vector. While the structure of the model remains constant, training and evaluation are performed separately for each individual source-detector separation.

To further assess the robustness of the model, we performed an additional validation analysis in which the model was tested on flow rate combinations that were never part of the training data. In this analysis, we used the $g_2(r, \tau)$ data obtained at a source-detector separation of 1 cm and randomly selected 5, 10, 20, 30, and 50% of the flow rate combinations out of the total 134 combinations. The measured $g_2(r, \tau)$ data corresponding to these selected flow rates were used exclusively for validation, and the model was trained with the other $g_2(r, \tau)$ data.

Table 1 shows all the parameters used for the proposed LSTM design in this study. Our model consists of two hidden LSTM layers, each with 512 LSTM memory units. The mean squared error (MSE) loss function was used as the loss function during the training phase, and adaptive moment estimation (Adam) was used as the optimizer. Initially, the learning rate was set at 1×10^{-4} . The batch size and epoch number were set to 501 and 200, respectively. We also

applied a dropout rate of 0.1 to avoid overfitting. The model was developed in Python using Pytorch and executed on an Nvidia K80 GPU with 12 GB GPU memory and a GPU memory clock of 0.82 GHz.

Table 1. Parameters of the proposed LSTM model

Parameters	Specified Values
Input size	1×167
LSTM hidden layer number	2
LSTM unit in each layer	512
Loss Function	MSE
Learning rate	0.0001
Optimizer	Adam
Batch size	501
Epoch	200
Output size	1×2

We used the root mean squared error (RMSE; Eqs. (5) and (6)), mean absolute error (MAE; Eq. (7)), and their percentages (RMSE% and MAE%; Eqs. (8) and (9), respectively) to evaluate the prediction performances of the flow rates and compare our results with prior research.

$$MSE = \frac{\sum_{i=1}^N (FR_{meas} - FR_{pred})^2}{N} \quad (5)$$

$$RMSE = \sqrt{MSE} \quad (6)$$

$$MAE = \frac{\sum_{i=1}^N |FR_{meas} - FR_{pred}|}{N} \quad (7)$$

$$RMSE\% = \frac{RMSE}{\frac{1}{N} \sum_{i=1}^N FR_{meas}} \times 100 \quad (8)$$

$$MAE\% = \frac{MAE}{\frac{1}{N} \sum_{i=1}^N FR_{meas}} \times 100 \quad (9)$$

Here, N represents the total number of samples in the test data, and FR_{meas} and FR_{pred} represent the true flow rate measured by the outflow of the flow phantom and the predicted rate calculated by our model, respectively.

Additionally, we calculated the square of Pearson correlation coefficient (R^2 value) between the measured and predicted flow rates. To compare the accuracy of deep tissue blood flow detection between the machine-learning-based approach and the semi-infinite BFI approach, we also calculated the R^2 value between the deep layer flow rates and BFI values obtained at source-detector separations of 2 and 3 cm.

2.4.3. Monte Carlo simulation based robustness evaluation to changes in optical and anatomical parameters

We conducted an additional simulation-based investigation to assess the robustness of the proposed model to variations in anatomical structures and optical properties, considering the potential application of this method for in vivo measurements of biological tissues. This experiment employed a Monte Carlo based photon propagation simulation of a two-layer physics-based model [37]. We utilized Monte Carlo eXtreme (MCX) software for the photon propagation simulation [38].

We trained the deep-learning-based model using 250 autocorrelation functions derived from 25 combinations of flow rates in the shallow and deep layers. These combinations include all possible permutations of 0, 10, 20, 40, and 60 ml/min/100 g of simulated tissue, with 10 observations obtained for each combination. Since the precise relationship between the flow rates and αD_B values in each layer remains unknown, we defined $\alpha D_B = 1 \times 10^{-6} \text{ mm}^2/\text{s}$ as equivalent to 1 ml/min/100 g of simulated tissue in this simulation. The 90% of simulated data were used for training, while the remaining 10% was employed to verify the prediction accuracy of the trained model.

The test dataset was generated under fixed flow rates of (shallow, deep) = (10, 20) ml/min/100 g of simulated tissue. For each set of the following seven conditions, ten simulations were conducted: (1) original optical and anatomical conditions, (2) 10% larger and (3) 10% smaller absorption coefficient conditions in the deep layer, (4) 10% larger and (5) 10% smaller reduced scattering coefficient conditions in the deep layer, and (6) 1 mm thicker and (7) 1 mm thinner shallow layer depth conditions. The depth of shallow layer was remained at its original value of 5.5 mm in conditions (1)-(5), and the optical parameters were kept at their original values in conditions (6) and (7). Using the trained model, the flow rates in the shallow and deep layers were estimated and the mean relative change ratio of the predicted flow rates to those obtained in condition (1) was evaluated.

3. Results

3.1. Autocorrelation function characteristics for different shallow and deep-layer flow rates measured at different DCS source-detector separations

The observed photon count rates per second were $3.57 \times 10^6 \pm 3.90 \times 10^3$, $2.90 \times 10^5 \pm 437$, and $2.42 \times 10^4 \pm 40$ (mean \pm standard error) at source-detector separations of 1, 2, and 3 cm, respectively. Figures 3 and 4 show the effect of different flow rates in the shallow and deep layers on the autocorrelation function $g_1(r, \tau)$, measured under two constant flow rate conditions for the deep and shallow layers, respectively, at various DCS source-detector separations.

The slopes of $g_1(r, \tau)$ exhibited clear differentiation across flow rates in the shallow layer, regardless of the source-detector separation, under the condition of a modest flow rate in the deep layer (10 ml/min/100 g of simulated tissue; Figs. 3(a) to 3(c)). However, when the flow rate of the deep layer was increased to 60 ml/min/100 g of simulated tissue, the slopes of the $g_1(r, \tau)$ generally increased regardless of the flow rate in the shallow layer (Figs. 3(d) to 3(f)). Furthermore, the differentiation in the $g_1(r, \tau)$ slopes among the varied flow rates in the shallow layer became less pronounced, particularly for the channels with long source-detector separations (Fig. 3(f)).

When the flow rates of the deep layer were varied under the constant and moderate flow rate of the shallow layer (5 ml/min/100 g of simulated tissue; Figs. 4(a) to 4(c)), the differentiation in the slopes of the $g_1(r, \tau)$ functions became more apparent in channels with source-detector separations of 2 and 3 cm compared to the 1 cm channel separation. This relationship remained consistent even when the flow rate in the shallow layer was increased (Figs. 4(d) to 4(f)), although the differentiation in slopes across different flow rates in the deep layer became smaller (Figs. 4(e) and 4(f)).

3.2. Effect of shallow and deep tissue flow rates on the estimated BFI values

In this section, we examined the impact of flow rate in the shallow and deep layers on the estimated BFI values with different source-detector separations. Figure 5 shows the relationships between the BFI values and flow rates of the shallow and deep layers. We found that the following linear relationships exist between the BFI values and flow rates at any condition of source-detector

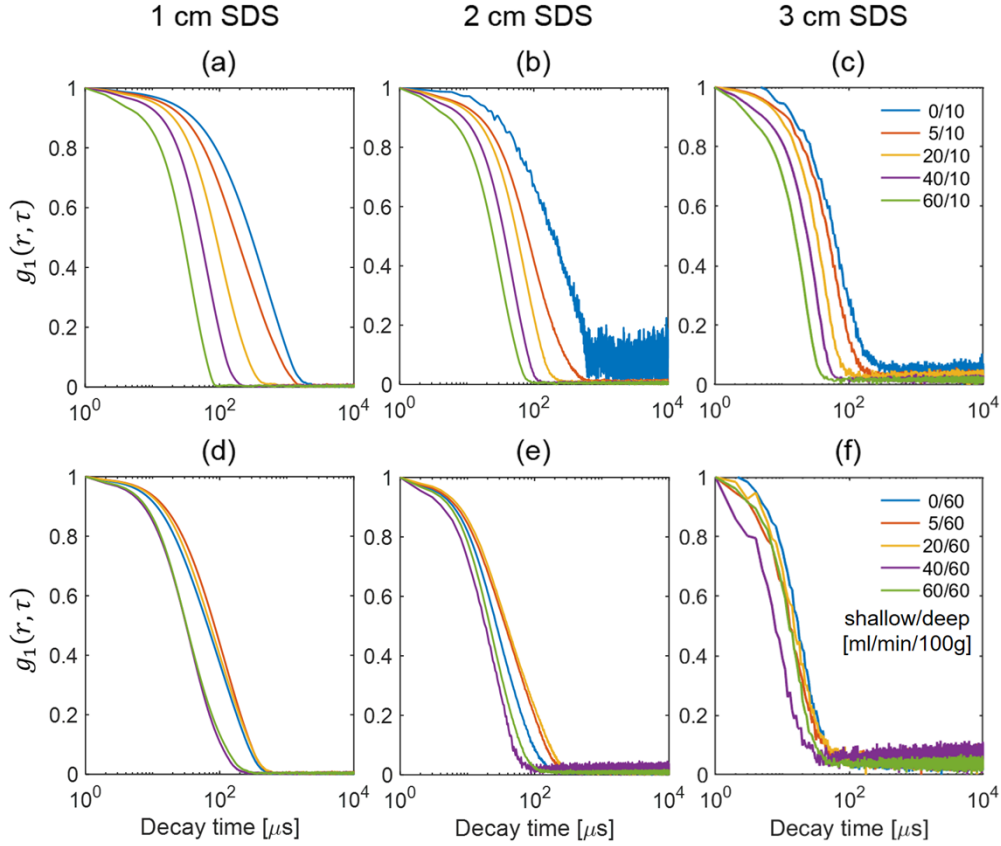


Fig. 3. Changes in $g_1(r, \tau)$ slopes with varied shallow-layer flow rates under a fixed deep-layer flow rate. The deep-layer flow rate was fixed to 10 and 60 ml/min/100 g of simulated tissue in (a)-(c) and (d)-(f), respectively. The source-detector separation was 1 cm for (a) and (d), 2 cm for (b) and (e), and 3 cm for (c) and (f). SDS: source-detector separation.

separation.

$$BFI_{SD\ 1\ cm} = 0.804 \cdot FR_{shallow} + 0.113 \cdot FR_{deep} + 3.300 \quad (10)$$

$$BFI_{SD\ 2\ cm} = 0.969 \cdot FR_{shallow} + 0.373 \cdot FR_{deep} + 4.949 \quad (11)$$

$$BFI_{SD\ 3\ cm} = 1.359 \cdot FR_{shallow} + 0.624 \cdot FR_{deep} + 6.988 \quad (12)$$

The R^2 values for the linear approximation were 0.947, 0.930, and 0.914 for the source-detector separations of 1, 2, and 3 cm, respectively.

The determined linear relationship between the BFI values and flow rates of the shallow and deep layers suggests that different combinations of shallow and deep flow rates could result in the same BFI value. The red dots shown in Figs. 5(a) to 5(c) represent two data points with comparable BFI values at the corresponding source-detector separation condition, although these BFI values were derived from different combinations of flow rates in the shallow and deep layers. Figures 5(d) to 5(f) show the superposition of $g_1(r, \tau)$ obtained at the source-detector separation for the selected data points. Although $g_1(r, \tau)$ produced nearly identical BFI values for the different flow rates in the shallow and deep layers; these data points did not overlap exactly at any source-detector separation.

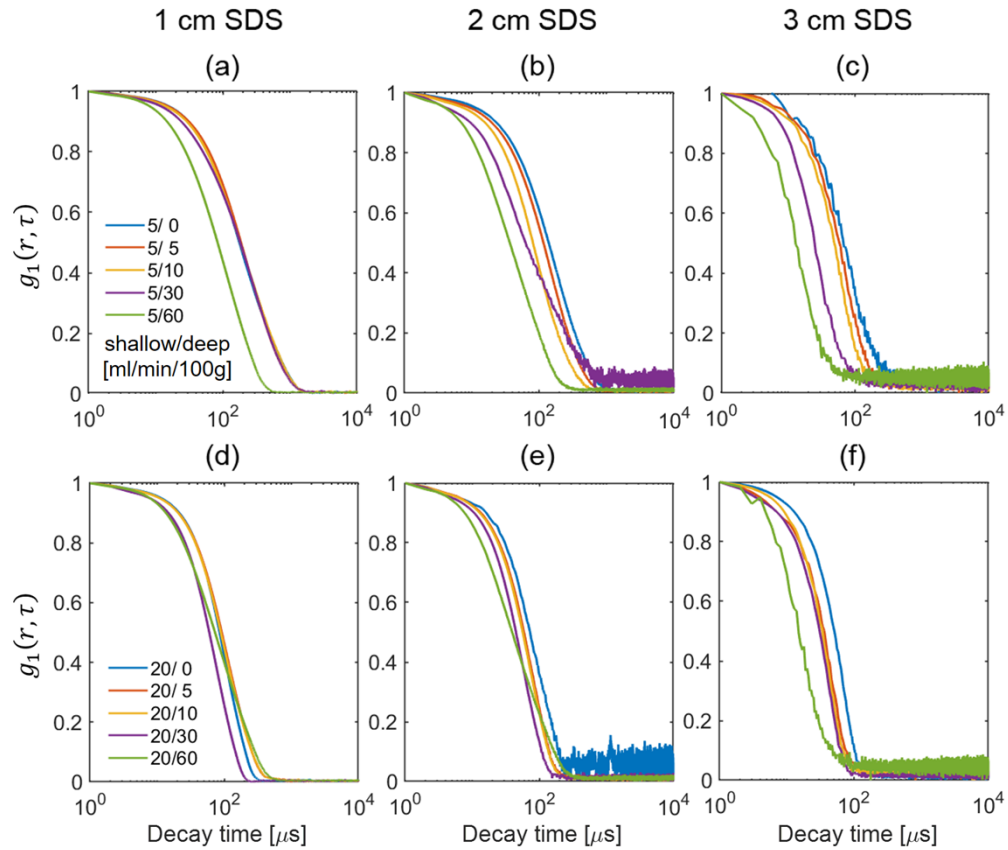


Fig. 4. Changes in $g_1(r, \tau)$ slopes with varied deep-layer flow rates under a fixed shallow-layer flow rate. The shallow-layer flow rate was fixed to 5 and 20 ml/min/100 g of simulated tissue in (a)-(c) and (d)-(f), respectively. The source-detector separation was 1 cm for (a) and (d), 2 cm for (b) and (e), and 3 cm for (c) and (f). SDS: source-detector separation.

3.3. Prediction accuracy of the shallow and deep flow rates

Figure 6 illustrates the predicted flow rates of 134 test datasets by the LSTM model superimposed on the measured flow rates, which were determined using $g_2(r, \tau)$ at a source-detector separation of 2 cm. Generally, the predicted and measured flow rates showed a good agreement regardless of the flow rates within the range used in the current study. Interestingly, the prediction accuracies were comparable when either all three or only one of the $g_2(r, \tau)$ systems that were measured simultaneously at the three different source-detector separations were used to predict the flow rates (Table 2). The square of Pearson's correlation coefficients between the measured and predicted flow rates were more than 0.99 in both the shallow and deep layers, regardless of the use of three or one $g_2(r, \tau)$ system for prediction. The R^2 values between the BFI and the measured deep layer flow rates were 0.74 and 0.82 for inter-probe intervals of 2 and 3 cm, respectively, demonstrating the excellent performance of machine-learning based prediction of deep tissue blood flow over the semi-infinite BFI-based approach.

The prediction performances are summarized in Table 2 with comparisons to the results of previous studies that applied deep learning to predict blood flow rate using the DCS method [20–24,39]. The comparison suggests that our proposed system performs better than all previous studies in all evaluation criteria. The robustness of the model was further confirmed in the

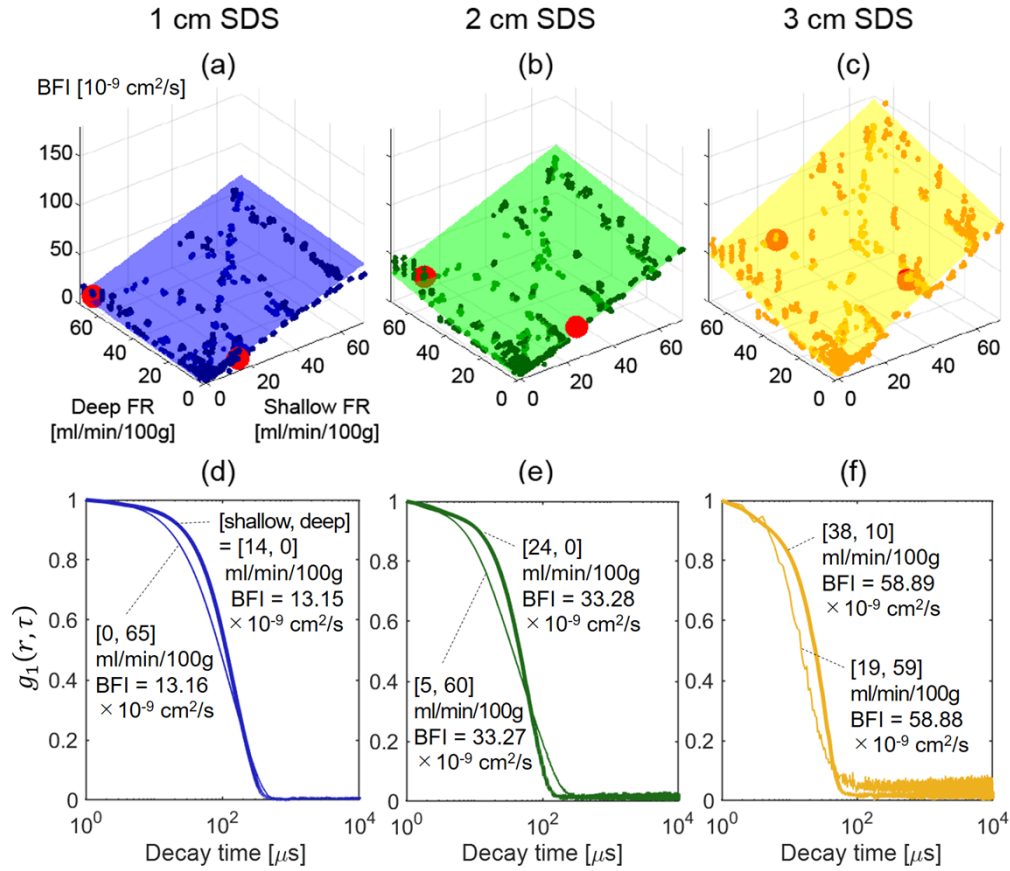


Fig. 5. Linear relationship between the BFI and flow rate, and examples of $g_1(r, \tau)$ showing equivalent BFI values that emerged from different combinations of shallow and deep flow rates. FR: flow rate, SDS: source-detector separation.

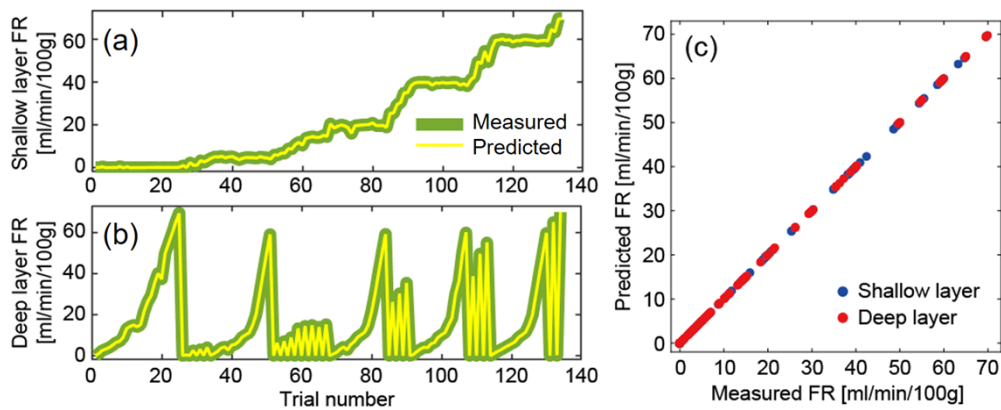


Fig. 6. Correlations between the measured and predicted flow rates in 134 test datasets for the autocorrelation function $g_2(r, \tau)$ measured at a source-detector separation of 2 cm. These autocorrelation functions were never used to develop a classifier. (a) Comparisons of the shallow-layer flow rates; (b) comparisons of the deep-layer flow rates; (c) correlation of the measured and predicted flow rates in both layers. FR: flow rate.

Table 2. Prediction performance summary of the proposed and previously developed deep-learning-based DCS blood flow estimation methods using phantom models^a

Author	Model	Output	Data size	RMSE/RMSE%	MAE/MAE%	R ² value
Zhang et al. [20]	RNN, regression model	BFI	NA	2.22/NA	NA/NA	NA
Zhang et al. [39]	Support vector regression	BFI	NA	2.33/NA	NA/NA	NA
Li et al. [22]	LSTM	BFI	30000 × 64	NA/3.3%	NA/2.18%	0.95
Proposed model	LSTM	FR	4020 × 501	Shallow layer	Shallow layer	Shallow layer
				0.072/0.32%	0.058/0.26%	0.99
				Deep layer	Deep layer	Deep layer
				0.067/0.41%	0.049/0.31%	0.99
		FR	1340 × 501 SD = 1 cm	Shallow layer	Shallow layer	Shallow layer
				0.044/0.20%	0.029/0.27%	0.99
				Deep layer	Deep layer	Deep layer
				0.044/0.13%	0.033/0.21%	0.99
		FR	1340 × 501 SD = 2 cm	Shallow layer	Shallow layer	Shallow layer
				0.047/0.21%	0.036/0.21%	0.99
				Deep layer	Deep layer	Deep layer
				0.034/0.16%	0.026/0.16%	0.99
		FR	1340 × 501 SD = 3 cm	Shallow layer	Shallow layer	Shallow Layer
				0.096/0.43%	0.068/0.36%	0.99
				Deep layer	Deep layer	Deep layer
				0.058/0.30%	0.041/0.26%	0.99

^aBFI: blood flow index, FR: flow rate, NA: not available, SD: source-detector separation.

additional validation analysis in which the shallow and deep layer flow rates of $g_2(r, \tau)$ data can be accurately estimated even though the corresponding flow rate combinations were not included in the training dataset (Table 3). The RMSE and MAE increased approximately fourfold when the target flow rate combinations were not included in the training dataset. However, the error value was still less than 0.2 ml/min/100 g of simulated tissue and the results maintained an excellent correlation between the measured and predicted flow rates, which is acceptable for practical measurement of active muscle blood flow [29–36]. Overall, these results indicate that our proposed system can continuously predict and accurately monitor blood flow rate.

3.4. Robustness evaluation to changes in optical and anatomical parameters

The prediction performances of the deep-learning-based model that was trained with the simulated autocorrelation function dataset are summarized in Table 4. Although the number of training datasets was smaller than those collected in the physical phantom experiment, the proposed model showed sufficient prediction performance of flow rates in both layers (Table 4).

The prediction results showed that the changes in optical or anatomical parameters affected the predicted flow rates as expected, with more pronounced effects particularly in the shallow layer

Table 3. Changes in prediction performance of the proposed model with reduced flow rate combinations in training data^a

	Random 90-10 split (Table 2)	5% of FR combination reduction	10% of FR combination reduction	20% of FR combination reduction	30% of FR combination reduction	50% of FR combination reduction
RMSE	0.044/ 0.044	0.105/ 0.071	0.157/ 0.103	0.163/ 0.121	0.175/ 0.144	0.183/ 0.135
MAE	0.029/ 0.033	0.061/ 0.054	0.124/ 0.085	0.131/ 0.091	0.137/ 0.101	0.142/ 0.099
R ² value	0.99/ 0.99	0.99/ 0.99	0.99/ 0.99	0.99/ 0.99	0.99/ 0.99	0.99/ 0.99

^aFR: flow rate. First and second rows in each cell correspond to performance measures determined with shallow and deep layer flow rates, respectively. All performance measures were derived from autocorrelation functions measured at 1 cm source-detector separation.

Table 4. Prediction performance summary of the proposed deep-learning-based DCS blood flow estimation method trained with autocorrelation functions derived from two-layer slab model of Monte Carlo based simulation.

	Shallow layer	Deep layer
RMSE	0.18	0.22
MAE	0.15	0.18
R ²	0.99	0.99

(Fig. 7). However, the absolute changes were less than 3% of the flow rate, suggesting a relatively small impact when considering the dynamic range of blood flow changes typically observed in active muscles [29–36].

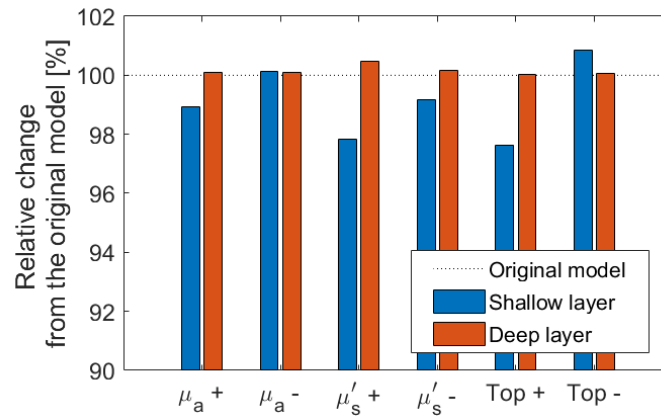


Fig. 7. Relative change in the predicted flow rates in the shallow (blue) and deep (red) layers obtained from simulated autocorrelation functions with slightly modified optical and anatomical parameters. $\mu_a +$ and $-$ represent conditions with 10% increased and decreased absorption coefficient in the deep layer, $\mu'_s +$ and $-$ represent conditions with 10% increased and decreased reduced scattering coefficient in the deep layer, and Top + and $-$ represent 1 mm thicker and thinner depth of the shallow layer, respectively.

4. Discussion

The objective of the current study was twofold. First, we used a two-layer flow phantom to investigate how changes in flow rate in the shallow and deep layers affected the morphology of $g_1(r, \tau)$ and the derived BFI values. Our results showed that the effects of flow rate variations on the $g_1(r, \tau)$ and BFI values differed depending on the source-detector separation, which reflects the nature of continuous-wave DCS measurements that include the effect of photon displacements at any depth on the optical pathlength. Second, we aimed to predict the flow rates of the shallow and deep layers using machine learning techniques based on the different impacts of shallow and deep-layer flow rates on $g_2(r, \tau)$. Our approach showed promising results, demonstrating excellent agreement between the predicted and measured flow rates. Therefore, a deep-learning-based blood flow estimation method could be a useful tool for determining the blood flow information of cutaneous and muscle tissues in DCS measurements.

The comparison of the $g_1(r, \tau)$ results obtained under various flow rates in the shallow layer while with a constant flow rate in the deep layer demonstrates that the slopes of $g_1(r, \tau)$ and the corresponding BFI values are affected by changes in the shallow-layer flow rate, especially when the deep layer flow rate is slow. In physiological measurements of muscle or cerebral blood flow using DCS, changes in cutaneous blood flow must be carefully monitored or controlled as they significantly affect BFI values [11,12]. This is especially important in muscle blood flow measurements during exercise when the increase in muscle blood flow further causes the local warming of tissue to increase cutaneous blood flow. The contribution of cutaneous and muscle blood flow increments to the increased BFI values must be precisely separated to prevent the overestimation of exercise-related muscle blood flow changes.

The effectiveness of longer source-detector separations in capturing changes in deep layer flow rates was observed in the comparisons of the $g_1(r, \tau)$ and BFI values when varying the deep-layer flow rates under a constant shallow-layer flow rate. The slopes of $g_1(r, \tau)$ showed good separation depending on the deep-layer flow rate at 2- and 3-cm source-detector separations when the shallow-layer flow rate was constant and slow (5 ml/min/100 g of simulated tissue), while the $g_1(r, \tau)$ results mostly overlapped at a source-detector separation of 1 cm, regardless of the flow rates in the deep layer. These phenomena are attributed to the fact that the DCS probe settings with small source-detector separations mostly capture photons that have traveled through shallow layers, while those with large separations could capture photons that have traveled through both shallow and deep layers, supporting the previously reported relationship between measurable depth and source-detector separation in DCS measurements [40–42]. However, the resolution of the deep-layer flow rates in the autocorrelation functions was interfered with if the shallow layer had faster flow rates, the effect of which is more severe in the shorter source-detector separation conditions.

The estimated BFI values showed a good linear relationship with the flow rates of the shallow and deep layers, whose slope increased along with the length of source-detector separation. These results suggest the better sensitivity of DCS measurement at longer source-detector separations in quantifying flow rate. The linear relationship also suggests that the same BFI value could apply to various combinations of shallow and deep-layer flow rates. Therefore, we further investigated the detailed morphology of $g_1(r, \tau)$ which emerged with nearly identical BFI values. Our observations indicate that the flow rates in the shallow and deep layers independently contribute to the shapes of $g_1(r, \tau)$, even though they share very close BFI values after the model fitting. The detailed differences in the $g_1(r, \tau)$ could have contributed to the excellent prediction accuracy of the LSTM network in predicting both shallow and deep-layer flow rates, even from single-channel DCS measurement.

Various deep-learning-based architectures such as CNN and RNN have been proposed to predict the BFI [20–22], denoising autocorrelation function [20,39], and blood-flow-related parameters [21,22,24]. We selected the LSTM network as it is the most feasible model for

capturing the features of the time sequences of the input data. Furthermore, it has been successfully implemented in the detection of BFI and other hemodynamic properties of tissues [22,23]. Consequently, the LSTM network was capable of differentiating $g_2(r, \tau)$ derived from different combinations of shallow and deep flow rates. Although a direct comparison is difficult to obtain based on differing experimental data and output parameters, the proposed LSTM network outperformed the previously reported BFI detection accuracy predicted by other machine-learning algorithms. Longer lengths of the input data and segmentation sizes and greater complexity in the LSTM layer may have contributed to a superior prediction performance relative to a similar LSTM-based model [22].

The errors in predicting flow rates were found to be negligible even when $g_2(r, \tau)$ was measured using a single source-detector separation. Interestingly, incorporating the simultaneously measured $g_2(r, \tau)$ data from various source-detector separations resulted in slightly worse prediction accuracies in most cases. These results are further supported by the fact that $g_2(r, \tau)$ contains the flow rate information of the shallow and deep layers at different ratios depending on the source-detector separation. Although the difference in the prediction accuracy is small, an independent classifier that solely considers $g_2(r, \tau)$ data obtained from a fixed source-detector separation may perform better than that which receives $g_2(r, \tau)$ data from multiple source-detector separations, which requires learning the different contributions of autocorrelation function morphologies associated with each separation dataset. However, an exception was found in the shallow-layer flow rate, where combining multiple $g_2(r, \tau)$ data relative to the single $g_2(r, \tau)$ data at a source-detector separation of 3 cm resulted in improved prediction accuracy. This suggests that the $g_2(r, \tau)$ data obtained at long source-detector separations are less sensitive to shallow-layer flow rates, and that the addition of $g_2(r, \tau)$ data obtained from multiple source-detector separations compensates for this lack of sensitivity.

There are several limitations to consider when interpreting the results of this study. First, the practical accuracy of the proposed method in differentiating cutaneous and muscle blood flow needs to be further tested using a more realistic phantom that models the DCS particle displacement as diffusion of a dense colloidal fluid [43,44] and in vivo experiments with controlled cutaneous blood flow [10,11]. We observed that the decay rates of the autocorrelation function were not in accordance with the flow velocity order in some of the faster flow settings within the deep layer. This may indicate potential flow rate heterogeneity due to the structure of the phantom. Second, the analytical BFI values were derived with a simple homogeneous semi-infinite plate medium model. While a multi-layer analytical correlation diffusion model has been increasingly used in DCS simulations and static phantom studies for inhomogeneous tissues [16–19,37], we found that optimization of the current flow phantom data to this analytical model consistently converged to a small BFI value (approximately $1.2 \times 10^{-9} \text{ cm}^2/\text{s}$), particularly in the deep layer (data not shown). This observation suggests that subtle differences in the decay characteristics of the autocorrelation functions between the analytical and experimental data may lead to estimation errors, as has been reported for in vivo measurement data [16]. This highlights the need for further validation of this method using more realistic phantom models or in vivo studies. Additionally, the current LSTM network can only be applied to biological tissues with similar anatomical structures and optical properties. Although our Monte Carlo based simulations suggest robustness to small changes in the optical or anatomical parameters of the target tissue, a comprehensive exploration of prediction errors for all combinations of flow rates has not been conducted. Therefore, the prediction results should be interpreted with caution. Future studies could explore optimal parameters in Monte Carlo simulations to replicate the autocorrelation functions obtained with the real flow phantom settings. If the simulated dataset could be used to train the predictor of biological tissue measurements, a personalized LSTM model could be developed to provide more precise cutaneous and muscle blood flow estimations.

5. Conclusion

This study investigated the effects of flow rate changes on the morphology of autocorrelation functions and the derived BFI values in a two-layer flow phantom. We investigated the potential of using machine-learning techniques to predict the flow rates of shallow and deep tissue layers. Our findings indicated that the changes in the shallow- and deep-layer flow rates and the source-detector separation have varied impacts on the slopes of autocorrelation functions and BFI values. The linear relationship between the flow rates and BFI values suggests that model-fit-based BFI detection may suffer from misinterpreting changes in cutaneous and muscle blood flow. Finally, our machine learning approach showed promising results in detecting the different contributions of shallow- and deep-layer flow rates considering the autocorrelation function used to predict both of these flow rates. Overall, our study highlights the potential of combining DCS measurements with machine learning techniques to improve blood flow estimation in applications such as active muscle measurements.

Funding. Japan Society for the Promotion of Science (20K21772, 21K11457, 21K19738, 23H03288).

Disclosures. The authors declare no conflicts of interest.

Data availability. Data underlying the results presented in this paper are available in [Dataset 1](#), Ref. [45].

References

1. G. Yu, "Near-infrared diffuse correlation spectroscopy in cancer diagnosis and therapy monitoring," *J. Biomed. Opt.* **17**(1), 010901 (2012).
2. Y. Shang, K. Gurley, and G. Yu, "Diffuse correlation spectroscopy (DCS) for assessment of tissue blood flow in skeletal muscle: recent progress," *Anat. Physiol.* **3**(2), 128 (2013).
3. E. M. Buckley, A. B. Parthasarathy, P. E. Grant, A. G. Yodh, and M. A. Franceschini, "Diffuse correlation spectroscopy for measurement of cerebral blood flow: future prospects," *Neurophotonics* **1**(1), 011009 (2014).
4. T. Durduran and A. G. Yodh, "Diffuse correlation spectroscopy for non-invasive, micro-vascular cerebral blood flow measurement," *NeuroImage* **85**(1), 51–63 (2014).
5. Y. Shang, T. Li, and G. Yu, "Clinical applications of near-infrared diffuse correlation spectroscopy and tomography for tissue blood flow monitoring and imaging," *Physiol. Meas.* **38**(4), R1–R26 (2017).
6. M. Ichinose, M. Nakabayashi, and Y. Ono, "Sympathoexcitation constrains vasodilation in the human skeletal muscle microvasculature during postocclusive reactive hyperemia," *Am. J. Physiol. Heart Circ. Physiol.* **315**(2), H242–H253 (2018).
7. W. J. Tucker, R. Rosenberry, D. Trojacek, H. H. Chamseddine, C. A. Arena-Marshall, Y. Zhu, J. Wang, J. M. Kellawan, M. J. Haykowsky, F. Tian, and M. D. Nelson, "Studies into the determinants of skeletal muscle oxygen consumption: novel insight from near-infrared diffuse correlation spectroscopy," *J. Physiol.* **597**(11), 2887–2901 (2019).
8. R. Rosenberry, W. J. Tucker, M. J. Haykowsky, D. Trojacek, H. H. Chamseddine, C. A. Arena-Marshall, Y. Zhu, J. Wang, J. M. Kellawan, F. Tian, and M. D. Nelson, "Determinants of skeletal muscle oxygen consumption assessed by near-infrared diffuse correlation spectroscopy during incremental handgrip exercise," *J. Appl. Physiol.* **127**(3), 698–706 (2019).
9. W. J. Tucker, R. Rosenberry, D. Trojacek, B. Sanchez, R. F. Bentley, M. J. Haykowsky, F. Tian, and M. D. Nelson, "Near-infrared diffuse correlation spectroscopy tracks changes in oxygen delivery and utilization during exercise with and without isolated arterial compression," *Am. J. Physiol. Regul. Integr. Comp. Physiol.* **318**(1), R81–R88 (2020).
10. M. Ichinose, M. Nakabayashi, and Y. Ono, "Rapid vasodilation within contracted skeletal muscle in humans: new insight from concurrent use of diffuse correlation spectroscopy and Doppler ultrasound," *Am. J. Physiol. Heart Circ. Physiol.* **320**(2), H654–H667 (2021).
11. M. F. Bartlett, J. D. Akins, A. P. Oneglia, R. M. Brothers, D. Wilkes, and M. D. Nelson, "Impact of cutaneous blood flow on NIR-DCS measures of skeletal muscle blood flow index," *J. Appl. Physiol.* **131**(3), 914–926 (2021).
12. M. F. Bartlett, A. Palmero-Canton, A. P. Oneglia, J. Mireles, R. M. Brothers, C. A. Trowbridge, D. Wilkes, and M. D. Nelson, "Epinephrine iontophoresis attenuates changes in skin blood flow and abolishes cutaneous contamination of near-infrared diffuse correlation spectroscopy estimations of muscle perfusion," *Am. J. Physiol. Regul. Integr. Comp. Physiol.* **324**(3), R368–R380 (2023).
13. G. Yu, T. F. Floyd, T. Durduran, C. Zhou, J. Wang, J. A. Detre, and A. G. Yodh, "Validation of diffuse correlation spectroscopy for muscle blood flow with concurrent arterial spin labeled perfusion MRI," *Opt. Express* **15**(3), 1064–1075 (2007).
14. D. Milej, L. He, A. Abdalmalak, W. B. Baker, U. C. Anazodo, M. Diop, S. Dolui, V. C. Kavuri, W. Pavlosky, L. Wang, R. Balu, J. A. Detre, O. Amendolia, F. Quattrone, W. A. Kofke, A. G. Yodh, and K. St Lawrence, "Quantification of cerebral blood flow in adults by contrast-enhanced near-infrared spectroscopy: validation against MRI," *J. Cereb. Blood Flow Metab.* **40**(8), 1672–1684 (2020).

15. T. Durduran, R. Choe, W. B. Baker, and A. G. Yodh, "Diffuse optics for tissue monitoring and tomography," *Rep. Prog. Phys.* **73**(7), 076701 (2010).
16. K. Verdecchia, M. Diop, A. Lee, L. B. Morrison, T. Y. Lee, and K. St. Lawrence, "Assessment of a multi-layered diffuse correlation spectroscopy method for monitoring cerebral blood flow in adults," *Biomed. Opt. Express* **7**(9), 3659–3674 (2016).
17. L. Gagnon, M. Desjardins, J. Jehanne-Lacasse, L. Bherer, and F. Lesage, "Investigation of diffuse correlation spectroscopy in multi-layered media including the human head," *Opt. Express* **16**(20), 15514–15530 (2008).
18. A. Kienle and T. Glanzmann, "In vivo determination of the optical properties of muscle with time-resolved reflectance using a layered model," *Phys. Med. Biol.* **44**(11), 2689–2702 (1999).
19. H. Zhao and E. M. Buckley, "Influence of source–detector separation on diffuse correlation spectroscopy measurements of cerebral blood flow with a multilayered analytical model," *Neurophotonics* **9**(03), 035002 (2022).
20. P. Zhang, Z. Gui, L. Hao, X. Zhang, C. Liu, and Y. Shang, "Signal processing for diffuse correlation spectroscopy using recurrent neural network of deep learning," in *IEEE Fifth International Conference on Big Data Computing Service and Applications*, 328–332 (2019).
21. J. Feng, M. Jiang, J. Bai, K. Jia, and Z. Li, "Cerebral blood flow monitoring using a ConvGRU model based on diffuse correlation spectroscopy," *Infrared Phys. Technol.* **129**, 104541 (2023).
22. Z. Li, Q. Ge, J. Feng, K. Jia, and J. Zhao, "Quantification of blood flow index in diffuse correlation spectroscopy using long short-term memory architecture," *Biomed. Opt. Express* **12**(7), 4131–4146 (2021).
23. Z. Li, M. Jiang, J. Feng, and K. Jia, "Quantification of blood flow and oxygen saturation based on multiwavelength diffuse correlation spectroscopy," *Proc. SPIE* **11900**, 119002U (2021).
24. C. S. Poon, F. Long, and U. Sunar, "Deep learning model for ultrafast quantification of blood flow in diffuse correlation spectroscopy," *Biomed. Opt. Express* **11**(10), 5557–5564 (2020).
25. J. Dong, R. Bi, J. H. Ho, P. S. P. Thong, K. C. Soo, and K. Lee, "Diffuse correlation spectroscopy with a fast Fourier transform-based software autocorrelator," *J. Biomed. Opt.* **17**(9), 0970041 (2012).
26. Y. Ono, K. Esaki, Y. Takahashi, M. Nakabayashi, M. Ichinose, and K. Lee, "Muscular blood flow responses as an early predictor of the severity of diabetic neuropathy at a later stage in streptozotocin-induced type I diabetic rats: a diffuse correlation spectroscopy study," *Biomed. Opt. Express* **9**(9), 4539–4551 (2018).
27. Y. Matsuda, M. Nakabayashi, T. Suzuki, S. Zhang, M. Ichinose, and Y. Ono, "Evaluation of local skeletal muscle blood flow in manipulative therapy by diffuse correlation spectroscopy," *Front. Bioeng. Biotechnol.* **9**, 800051 (2022).
28. M. Nakabayashi and Y. Ono, "Detection of blood flow speed in shallow and deep tissues using diffuse correlation spectroscopy," *Adv. Biomed. Eng.* **6**(0), 53–58 (2017).
29. K. E. Cooper, O. G. Edholm, and R. F. Mottram, "The blood flow in skin and muscle of the human forearm," *J. Physiol.* **128**(2), 258–267 (1955).
30. O. J. Hartling, H. Kelbaek, T. Gjørup, B. Schibye, K. Klausen, and J. Trap-Jensen, "Forearm oxygen uptake during maximal forearm dynamic exercise," *Eur. J. Appl. Physiol. Occup. Physiol.* **58**(5), 466–470 (1989).
31. L. I. Sinoway, J. Shenberger, J. Wilson, D. McLaughlin, T. Musch, and R. Zelis, "A 30-day forearm work protocol increases maximal forearm blood flow," *J. Appl. Physiol.* **62**(3), 1063–1067 (1987).
32. E. Blomstrand, G. Rådegran, and B. Saltin, "Maximum rate of oxygen uptake by human skeletal muscle in relation to maximal activities of enzymes in the Krebs cycle," *J. Physiol.* **501**(2), 455–460 (1997).
33. M. J. Joyner and D. P. Casey, "Regulation of increased blood flow (hyperemia) to muscles during exercise: a hierarchy of competing physiological needs," *Physiol. Rev.* **95**(2), 549–601 (2015).
34. P. G. Snell, W. H. Martin, J. C. Buckley, and C. G. Blomqvist, "Maximal vascular leg conductance in trained and untrained men," *J. Appl. Physiol.* **62**(2), 606–610 (1987).
35. T. Moritani, M. J. Berry, D. W. Bacharach, and E. Nakamura, "Gas exchange parameters, muscle blood flow and electromechanical properties of the plantar flexors," *Eur. J. Appl. Physiol. Occup. Physiol.* **56**(1), 30–37 (1987).
36. A. Kagaya, "Reduced exercise hyperaemia in calf muscles working at high contraction frequencies," *Eur. J. Appl. Physiol. Occup. Physiol.* **64**(4), 298–303 (1992).
37. M. M. Wu, S. T. Chan, D. Mazumder, D. Tamborini, K. A. Stephens, B. Deng, P. Farzam, J. Y. Chu, M. A. Franceschini, J. Z. Qu, and S. A. Carp, "Improved accuracy of cerebral blood flow quantification in the presence of systemic physiology cross-talk using multi-layer Monte Carlo modeling," *Neurophotonics* **8**(01), 015001 (2021).
38. Q. Fang and D. A. Boas, "Monte Carlo simulation of photon migration in 3D turbid media accelerated by graphics processing units," *Opt. Express* **17**(22), 20178–20190 (2009).
39. P. Zhang, Z. Gui, H. Ling, J. Liu, X. Zhang, Y. Liu, A. Li, and Y. Shang, "Signal processing for diffuse correlation spectroscopy with support vector regression," in *The Proceedings of the International Conference on Sensing and Imaging, 2018, Cham* (Springer International Publishing, 2019), pp. 173–184.
40. S. R. Arridge, M. Cope, and D. T. Delpy, "The theoretical basis for the determination of optical pathlengths in tissue: temporal and frequency analysis," *Phys. Med. Biol.* **37**(7), 1531–1560 (1992).
41. M. S. Patterson, S. Andersson-Engels, B. C. Wilson, and E. K. Osei, "Absorption spectroscopy in tissue-simulating materials: a theoretical and experimental study of photon paths," *Appl. Opt.* **34**(1), 22–30 (1995).
42. G. Yu, T. Durduran, G. Lech, C. Zhou, B. Chance, E. R. Mohler, and A. G. Yodh, "Time-dependent blood flow and oxygenation in human skeletal muscles measured with non-invasive near-infrared diffuse optical spectroscopies," *J. Biomed. Opt.* **10**(2), 024027 (2005).

43. D. A. Boas, S. Sakadžić, J. Selb, P. Farzam, M. A. Franceschini, and S. A. Carp, “Establishing the diffuse correlation spectroscopy signal relationship with blood flow,” *Neurophotonics* **3**(3), 031412 (2016).
44. E. Sathialingam, E. K. Williams, S. Y. Lee, C. E. McCracken, W. A. Lam, and E. M. Buckley, “Hematocrit significantly confounds diffuse correlation spectroscopy measurements of blood flow,” *Biomed. Opt. Express* **11**(8), 4786–4799 (2020).
45. M. Nakabayashi and Y. Ono, “Two-layer flow phantom DCS dataset,” figshare (2023), <https://doi.org/10.6084/m9.figshare.24133104>.